Journal of Power Sources 248 (2014) 196–204

Contents lists available at ScienceDirect

Journal of Power Sources

journal homepage: www.elsevier.com/locate/jpowsour

Stability of strontium-doped lanthanum manganite cathode in humidified air

Boxun Hu, Michael Keane, Manoj K. Mahapatra, Prabhakar Singh*

Center for Clean Energy Engineering, Department of Chemical, Materials and Biomolecular Engineering, University of Connecticut, 44 Weaver Road, Storrs, CT 06269-5233, USA

HIGHLIGHTS

- SrO segregates on LSM electrode surface in humidified air.
- SrO, $La_2Zr_2O_7$, and Mn_2O_3 form at the LSM/YSZ interfaces.
- Compound formation and segregation increase with water content and electric bias.
- Increased O_2 content reduces cathode degradation.

ARTICLE INFO

Article history:
Received 17 June 2013
Received in revised form
3 August 2013
Accepted 22 August 2013
Available online 14 September 2013

Keywords:
Strontium-doped lanthanum manganite
Degradation
SrO segregation
Humidified air
Oxygen partial pressure

ABSTRACT

The stability of strontium-doped lanthanum manganite (LSM) cathode has been studied using symmetric cells (humidified air, LSM/yttria-stabilized zirconia (YSZ)/LSM, humidified air) under a range of humidification levels (0–50%), temperatures (750–850 °C), and cathodic biases (0–0.5 V). Electrochemical impedance spectroscopy revealed an increase in non-ohmic resistance with increasing H_2O/O_2 ratio, temperature, and cathodic bias. Post-test surface and interface studies showed the segregation of SrO particles on the LSM surface and formation of Mn_2O_3 and $La_2Zr_2O_7$ compounds at the cathodic LSM/YSZ interface. The increase in non-ohmic resistance is attributed to surface segregation of SrO and interfacial compound formation, whereas formation and growth of SrO at the LSM surface is attributed to water adsorption. $La_2Zr_2O_7$ formation is attributed to interfacial reactions.

1. Introduction

Solid oxide fuel cells (SOFCs) are highly efficient electrochemical devices for energy conversion from hydrogen and hydrocarbon fuels [1–3]. The stability of SOFC components under various fabricating and operating conditions is crucial for long-term performance reliability and commercialization [4]. Strontium-doped lanthanum manganite (LSM) has been commonly used as a cathode material for SOFCs due to its high electrical conductivity and compatibility with yttria-stabilized zirconia (YSZ) electrolyte [5–7]. The interactions of impurities (H_2O, SO_2, and Cr vapor) with the LSM cathode have been investigated to increase SOFC durability [8–10]. Water vapor is a common constituent in air (~3 v%, all in volume) with higher content possible in coastal or tropical regions with heavy precipitation [11].

SOFCs containing an LSM cathode (140 kW peak power, Westinghouse) have demonstrated excellent stability with voltage degradation of less than 0.1%/kh during a 16,600-h test [12]. Haart et al. also reported a low degradation rate of approximately 20 mΩ cm^2/kh for short cell stacks containing LSM cathodes operated at 800 °C and a current density of 0.3 A cm^{-2} [13]. de Hagen et al. [14] reported that 4% humidified air makes an LSM-based SOFC operated at 750 °C and 0.5 A cm^{-2} perform worse and exhibit less durability, but this process is largely reversible when removing the humidity from air. For LSM-based SOFCs tested at 800 °C, Kim et al. [15] have reported voltage degradation of more than 10% and 20% during 2.5-h tests in 20% and 40% water vapor respectively, while no voltage degradation was reported in dry air.

Post-test characterization on electrically tested cells showed that degradation in humidified air is attributed to the formation of SrO, La_2O_3, or MnO_x, at the LSM cathode [4]. de Ridder et al. have

* Corresponding author. Tel.: +1 860 486 8379; fax: +1 860 486 8378.
E-mail address: singh@engr.uconn.edu (P. Singh).

0378-7753/$ – see front matter © 2013 Elsevier B.V. All rights reserved.
http://dx.doi.org/10.1016/j.jpowsour.2013.08.098

proven that impurity oxides at the YSZ surface decrease oxygen exchange using $^{16}O/^{18}O$ exchange experiments [16]. Several studies have also demonstrated that the LSM cathode performance was significantly improved after the passivation species (SrO) had been effectively removed or decreased by using acid etching, strontium deficient LSM, or cathodic current [17–19]. There is, however, no consensus on which metal oxide plays the most significant role in degradation. Jalili et al. have suggested that Sr enrichment is prevalent for the tensile-strained LSM surface at elevated temperatures [20]. Furthermore, Caillol et al. [21] and Huber et al. [22] have reported that the segregation of SrO may proceed at high temperatures and oxygen poor atmospheres or under cathodic polarization, but the evidence was not shown. Recently, Liu et al. have shown that water vapor (20%) promotes the decomposition of LSM cathode to form La_2O_3 and Mn_2O_3 [23]. Kim et al. similarly reported the segregation of La_2O_3 particles on the LSM surface in 40% water in air based on X-ray photoelectron spectroscopy (XPS) spectra of O1s and thermochemical calculations [15]. Mechanisms accounting for the role of water on the cathode degradation remain largely unknown.

In this study, we have investigated the stability of LSM cathode under a range of humidification levels, temperatures, and cathodic biases using a symmetric SOFC configuration [24]. A three-electrode configuration has allowed suitable measurements of cathodic impedance using electrochemical impedance spectroscopy (EIS) [25]. Surface and bulk analytical techniques, such as XPS, scanning electron microscopy, and X-ray diffraction were used to identify segregated compounds formed on the LSM cathodes and LSM/YSZ interfaces. The kinetics of cathodic oxygen reduction processes have been explained by the analyses of EIS using equivalent circuits. Reaction mechanisms involving water have been developed to explain the electrical performance degradation in humidified air.

2. Experimental

$(La_{0.8}Sr_{0.2})_{0.98}MnO_3$ (LSM) working and counter electrodes (thickness: ~17 μm, diameter: 1.0 cm) were screen-printed on both sides of a YSZ electrolyte ($(Y_2O_3)_{0.08}(ZrO_2)_{0.92}$, ~185 ± 25 μm thick) using LSM ink (Fuel Cell Materials). A reference electrode was similarly added near the periphery of the above electrolyte. After room temperature drying, the electrodes were sintered for 2 h at 1200 °C (heating rate of 3 °C min^{-1}) in air. Pt electrodes (diameter: 6 mm) were applied on both sides of the LSM electrodes using platinum mesh (Alfa Aesar) and platinum paste (Engelhard). The platinum paste was cured in air at 900 °C for 2 h (3 °C min^{-1}).

As-assembled LSM/YSZ/LSM symmetric cells were installed in a tubular alumina reaction chamber placed in the constant temperature zone of a furnace. The leads from a multi-channel potentiostat (VMP2, Bio-Logic) were connected to the three platinum electrodes of the symmetric cell. The schematic of the experimental setup is shown in Fig. 1. 3% water vapor was introduced in the air stream by flowing air through a water bubbler at room temperature. Higher humidification levels (10–50% water vapor) in the air stream, when needed, were introduced by injecting liquid water into the reaction chamber via a syringe pump (Harvard 360) with compressed air as the carrier gas (total flow 300 cm^3 min^{-1}). For dry air, two molecular sieve columns (length 0.6 m × 25 cm ID) were used for the removal of the moisture in compressed air.

To observe the effect of humidity level on short-term performance, LSM/YSZ/LSM symmetric cells were first operated in air (3% H_2O) for 12 h at 800 °C. An electrochemical impedance spectrum was subsequently recorded after establishing equilibrium condition of flow, temperature and humidity (approximately 1 h wait). For long-term stability tests, cells were tested under range of humidification levels (0–50%), temperatures (750–850 °C), and cathodic biases (0–0.5 V) up to 100 h. The real-time EIS were recorded by a multi-channel potentiostat at an interval of 2 h. A bias was applied between cathode and reference electrode in the frequency range from 0.5 Hz to 200 kHz with a 15 mV sinus amplitude. Similar experiments were conducted in an oxygen-containing atmosphere to compensate for the dilution of oxygen due to humidification. To maintain an oxygen level of 21% in humidified air (50% humidity level), we added 11 cm^3 min^{-1} O_2.

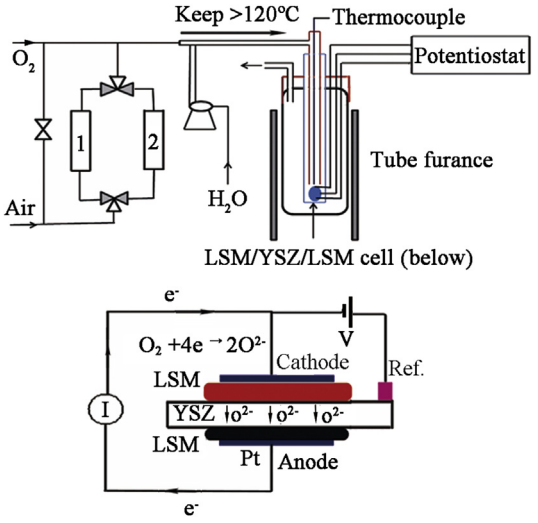

Fig. 1. The experimental setup for the stability tests of symmetric cells. Columns 1/2: molecular sieve columns.

Electrically tested cells were then analyzed for structural, morphological, and chemical changes. An FEI Quanta 250 FEG scanning electron microscope with an energy dispersive X-ray spectroscopy (EDS) system was used for the morphological and elemental analyses. A Bruker AXS D-8 Advance X-ray diffractometer (XRD) was used for the identification of phases present in both pre- and post-test cells. LaB_6 was used as a size/strain standard in XRD to calibrate instrumental broadening of diffraction peaks. The XPS measurements were carried out on a PHI 595 multiprobe system. The Al X-ray anode was run at 170 W with a pass energy of 100 eV at a scan rate of 1 eV/step for the survey scan and with a pass energy of 50 eV at a scan rate of 0.1 eV/step for the high resolution multiplex scan.

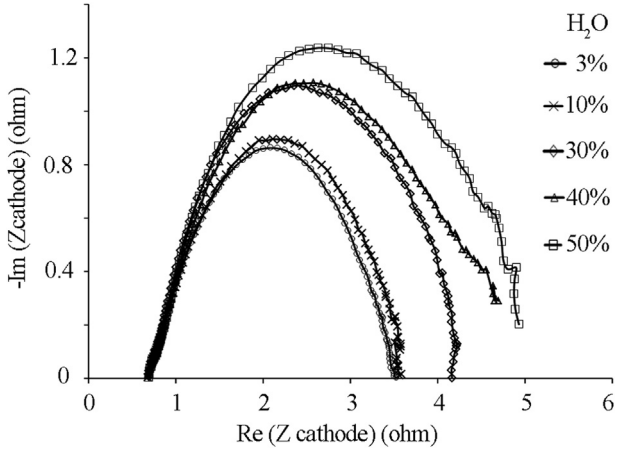

Fig. 2. EIS of LSM cathodes exposed to 3–50% water in air at 800 °C and 0.5 V bias.

3. Results

3.1. Electrical performance

Fig. 2 shows changes in the electrical performance behavior of LSM cathode exposed to various water containing atmospheres during 1-h tests at 800 °C. The non-ohmic resistance increases with higher water content, while the ohmic resistance remains unaffected by water content. During 100-h tests, higher water content accelerates changes in both ohmic and non-ohmic resistance leading to electrical performance degradation of the cathodes as shown in Fig. 3. During the initial exposure, a decrease in non-ohmic resistance (Rp) is observed (inset). Non-ohmic resistance increases with increasing water content. The Rp increases 0.1, 1.2, 6.4, and 22.2 Ω/100 h for the tests in 3%, 10%, 25%, and 50% H_2O, respectively. The ohmic resistance of the LSM cathode in 3% H_2O does not change with time. With the addition of oxygen to compensate for the dilution due to steam (keeping O_2 level at 21%), the Rp decreased from 22.2 Ω to 8.8 Ω. The ohmic resistance, on the other hand, slightly decreased from 1.1 Ω to 0.3 Ω in a 100-h test (data not shown).

Changes in the LSM cathode resistance during exposure to 750–850 °C are shown in Fig. 4. As observed, a large change in resistance is expected during long-term exposure at 850 °C. When compared to exposure at 750 °C, both ohmic and on-ohmic resistance remain stable at 750 °C, whereas non-ohmic resistance at 850 °C significantly increases after 100 h exposure. Ohmic resistance also increased from 2 Ω to 3 Ω at 850 °C, indicating fast degradation in humidified air.

The EIS spectra were analyzed using zSimpWin 3.30 to investigate the electrochemical reaction kinetics involving water and oxygen. An equivalent circuit ($R1(C2R2)(Q3R3)(C4R4)$) was developed through optimization. Comparison of the calculated and experimental data of the measured EIS spectra shows an excellent match (Fig. 5). $R1$ represents the ohmic resistance; ($C2R2$) is related to the adsorption and diffusion of oxygen species; ($Q3R3$) reflects the surface roughness, thickness, and heterogenous reactions such as the hydrolysis reaction; and ($C4R4$) stands for oxygen reduction [26]. Element values of equivalent circuits in Table 1 and Fig. 5 show the following trends in cathode degradation:

1. For the short-term (<3 h) tests at 800 °C, $R1$ does not change, while $R2$, $R3$, $C2$, and $C4$ increase with water content.
2. For the 100-h test at 850 °C in 50% water in air, the resistances increase in the following order: $R1 < R2 < R4 < R3$. $R3$ shows a rapid increase (Fig. 5).
3. Capacitance ($C2$ and $C4$) and the constant phase element initially decrease with time.

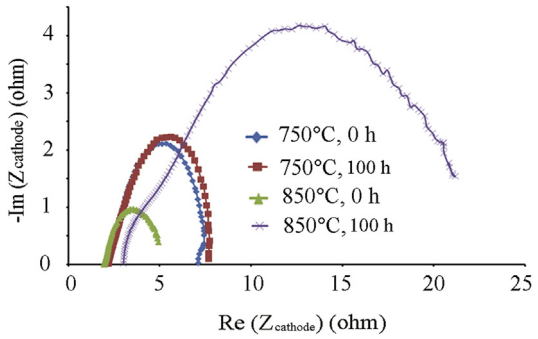

Fig. 4. EIS of LSM cathodes exposed in 50% water in air at different temperatures and 0.5 V bias for 100 h.

3.2. Morphology changes

The morphology of the polarized cathode surface and fresh sample were examined after the symmetric cells were tested in humidified (or dry) air with/without bias (Fig. 6). For the as-fabricated and untested LSM cathodes, smooth surfaces are observed (Fig. 6B). For the LSM cathode tested in dry air for 100 h in 750–850 °C temperature range and a 0.5 V bias, a smooth surface is observed, indicating no oxide segregation on the LSM surfaces.

Exposure of the LSM cathode to 50% water vapor at 750 and 850 °C without a bias showed the formation and segregation of nanoparticles on LSM cathode surfaces (Fig. 6E and F). The particle size increased with increasing temperature.

With an applied 0.5 V bias and at 850 °C, the size of the segregated particles on LSM cathodes increases with water content (Fig. 6G–I). Limited nanoparticles (20–30 nm) formed on the edges of LSM grains in air (3% water) (Fig. 6G). Increasing water content to 10%, additional nanoparticles in the size range of 30–40 nm formed more densely on the LSM surface and also inside the pores of the LSM cathode (Fig. 6H). When the water content increased to 50% with no additional oxygen, nanoparticles on LSM surfaces grew to larger sizes (60–80 nm) (Fig. 6I). Increase in oxygen content in the gas stream was found to retard the growth (Fig. 6J).

Fig. 7 shows morphological changes at the polarized interfaces of cathodic LSM/YSZ. The SEM image of the as-fabricated LSM/YSZ interface shows no secondary phase formation at the triple phase boundaries (TPB) as indicated in Fig. 7A. After electrical testing in dry air (Fig. 7B), TPB showed the formation of small particles. For the cells tested in air – 50% water atmosphere, the TPB's showed significant increase in the compound formation (Fig. 7C). The selected area EDS spectrum shows La, Zr, and O peaks, suggesting the formation of $La_2Zr_2O_7$.

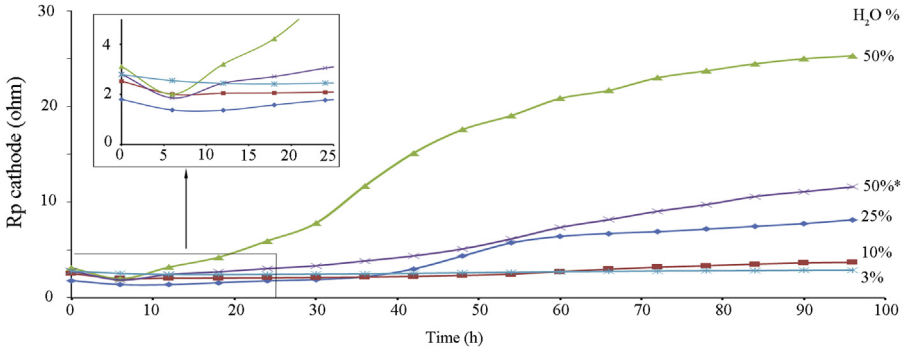

Fig. 3. The non-ohmic resistance–time plot of the LSM/YSZ/LSM cells in different water contents at 850 °C. "*" indicates oxygen added to keep the oxygen content at 21%.

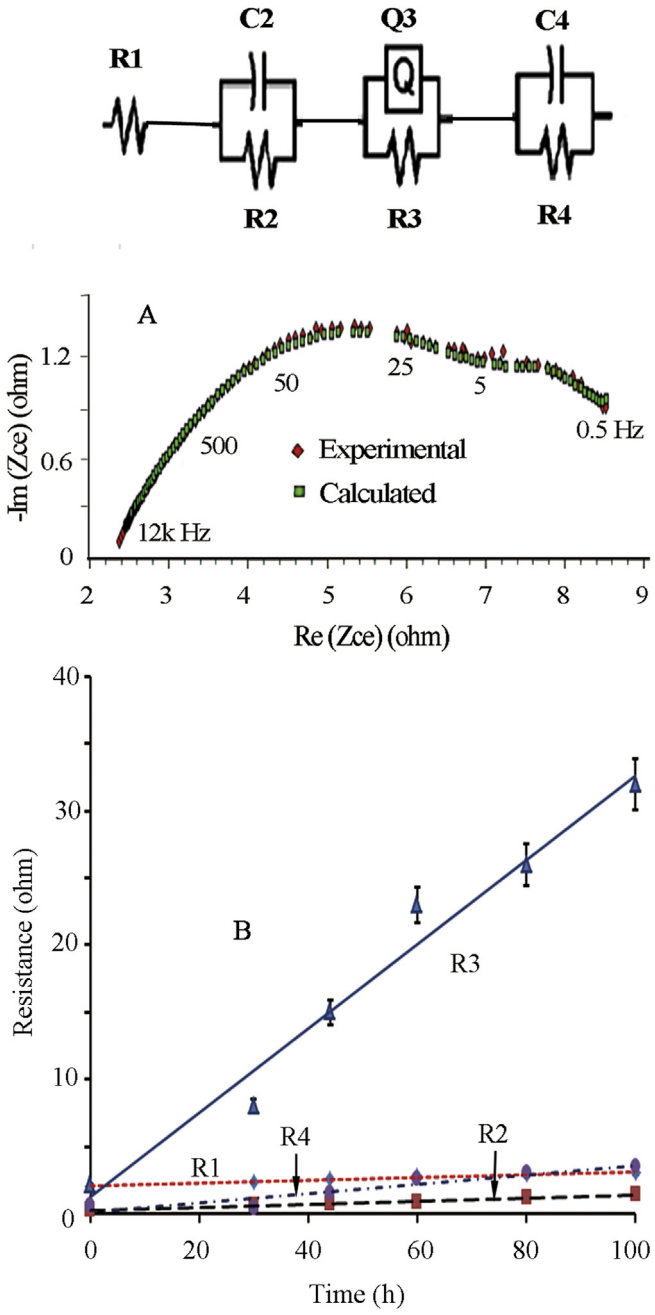

Fig. 5. An equivalent circuit model of the EIS in 50% water in air at 850 °C with a bias of 0.5 V and the resistance–time plots.

3.3. Characterization of compounds formation

The LSM cathode was removed from the YSZ electrolyte for XRD analysis. The compounds formed on the LSM electrodes were characterized by the XRD patterns shown in Fig. 8. For the cell operating in dry air and 3% H_2O/air at a temperature of 850 °C and a bias of 0.5 V, no evidence of secondary phases is shown. With subsequent increase in the humidity level to 10% in air, reaction products consisting of Sr $(OH)_2$, Mn_2O_3, and $La_2Zr_2O_7$ were observed in the XRD patterns of the LSM cathode/YSZ interface. When the water content was further increased to 50%, a similar XRD pattern was observed with higher peak intensities corresponding to the above reaction products. At 50% water content, the crystallite size of $Sr(OH)_2$ (at $2\theta = 24.8°$) is calculated using Scherrer Equation [27] to be ~42 nm, and the crystallite size of $La_2Zr_2O_7$ (at $2\theta = 43.1°$) is ~57 nm.

The XPS survey scan (Table 2) shows that the ratios of Sr/La and Sr/(Mn + La) at the surfaces of the post-test LSM cathodes are significantly increased compared to those of as-fabricated LSM samples, indicating Sr enrichment on the surfaces of these LSM cathodes. The molar ratio of Sr/(Mn + La) on the LSM surfaces slightly increased from 0.11 to 0.13 after calcination at 1200 °C for 2 h, and increased further to 0.21, 0.24, and 0.76 in 10%, 20%, and 50% water content, respectively. The shifts of binding energy are suggestive of the surface changes in chemical structure and compositions. The binding energy of Sr, 3d5/2 in the post-test samples is 132.8 eV, which is close to the literature value (133.0 eV) of $Sr(OH)_2$ [28]. The binding energy of Mn, 3d5/2 in the post-test samples is 642.0 eV, which is assigned to Mn_2O_3 (641.6 eV) [29]. The binding energy of La, 3d5/2 in the post-test samples is 835.1 eV, which is assigned to $La(OH)_3$ [30].

The SEM–EDS spectra of the as-fabricated and post-test LSM cathode surface (Fig. 9) show that the molar ratio of Sr/La on the LSM surface increased from 0.28 to 0.57 after testing in 50% H_2O in air with a bias of 0.5 V for 100 h, and the molar ratio of Sr/(Mn + La) increases from 0.13 to 0.33.

4. Discussion

Experiments performed under a wide range of humidification levels, temperatures, and cathodic bias conditions show three distinct features:

1. LSM cathodes are relatively stable in dry air or low water content and in the temperature range of 750–850 °C.
2. An increase in water content results in an increase in SrO particle segregation on LSM electrode surfaces at 750–850 °C with and without applied bias.
3. Cathode degradation is attributed to formation of SrO, $La_2Zr_2O_7$, and Mn_2O_3, which increase with water content, operating temperature, and electric bias (Table 3).

In dry exposure conditions with p_{O_2} in the range of 0.21–10^{-3} atm, LSM exhibits an oxygen excess nonstoichiometry

Table 1
Element values of the equivalent circuits corresponding to the EIS spectra.

Sample & conditions	*R*1 (Ω)	*C*2 (10^{-3} F)	*R*2 (Ω)	CPE (*n*) (S/s^n) 10^{-2}	*R*3 (Ω)	*C*4 (10^{-2} F)	*R*4 (Ω)
No. 1, 750 °C, 50% 100 h, 0.5 V	2.2 ± 0.02	2.0 ± 0.1	0.1 ± 0.01	1.6 ± 0.2 (0.76)	1.1 ± 0.1	2.2 ± 0.3	1.6 ± 0.1
No. 2, 0.5 V 800 °C-50%	0.7 ± 0.02	5.5 ± 0.1	0.5 ± 0.01	0.7 ± 0.1 (0.35)	2.0 ± 0.1	7.5 ± 0.1	0.5 ± 0.1
No. 2, 0.5 V 800 °C-30%	0.7 ± 0.02	4.7 ± 0.1	0.4 ± 0.01	1.7 ± 0.2 (0.62)	1.3 ± 0.1	6.3 ± 0.8	0.4 ± 0.1
No. 2, 0.5 V 800 °C-0%	0.7 ± 0.02	4.3 ± 0.1	0.2 ± 0.01	1.5 ± 0.1 (0.44)	0.8 ± 0.1	5.1 ± 0.4	0.3 ± 0.1
No. 3, 850 °C-50% 100 h, 0.5 V	3.0 ± 0.03	0.03 ± 0.0	1.4 ± 0.17	0.5 ± 0.1 (0.50)	32 ± 0.9	0.02 ± 0.0	3.5 ± 0.1
No. 3, 850 °C-50% 60 h, 0.5 V	2.8 ± 0.06	0.02 ± 0.0	0.8 ± 0.11	0.5 ± 0.1 (0.58)	23 ± 1.4	0.02 ± 0.0	2.6 ± 0.4
No. 3, 850 °C-50% 30 h, 0.5 V	2.4 ± 0.01	0.06 ± 0.0	0.6 ± 0.01	0.8 ± 0.1 (0.52)	8 ± 0.1	0.6 ± 0.1	0.4 ± 0.1
No. 3, 850 °C-50% 0 h, 0.5 V	2.0 ± 0.01	0.05 ± 0.0	0.3 ± 0.03	5.3 ± 0.1 (0.52)	2.1 ± 0.1	2.9 ± 0.1	0.6 ± 0.1

CPE: constant phase element, the value of the power (*n*) is in parenthesis. No addition O_2 was added in these tests.

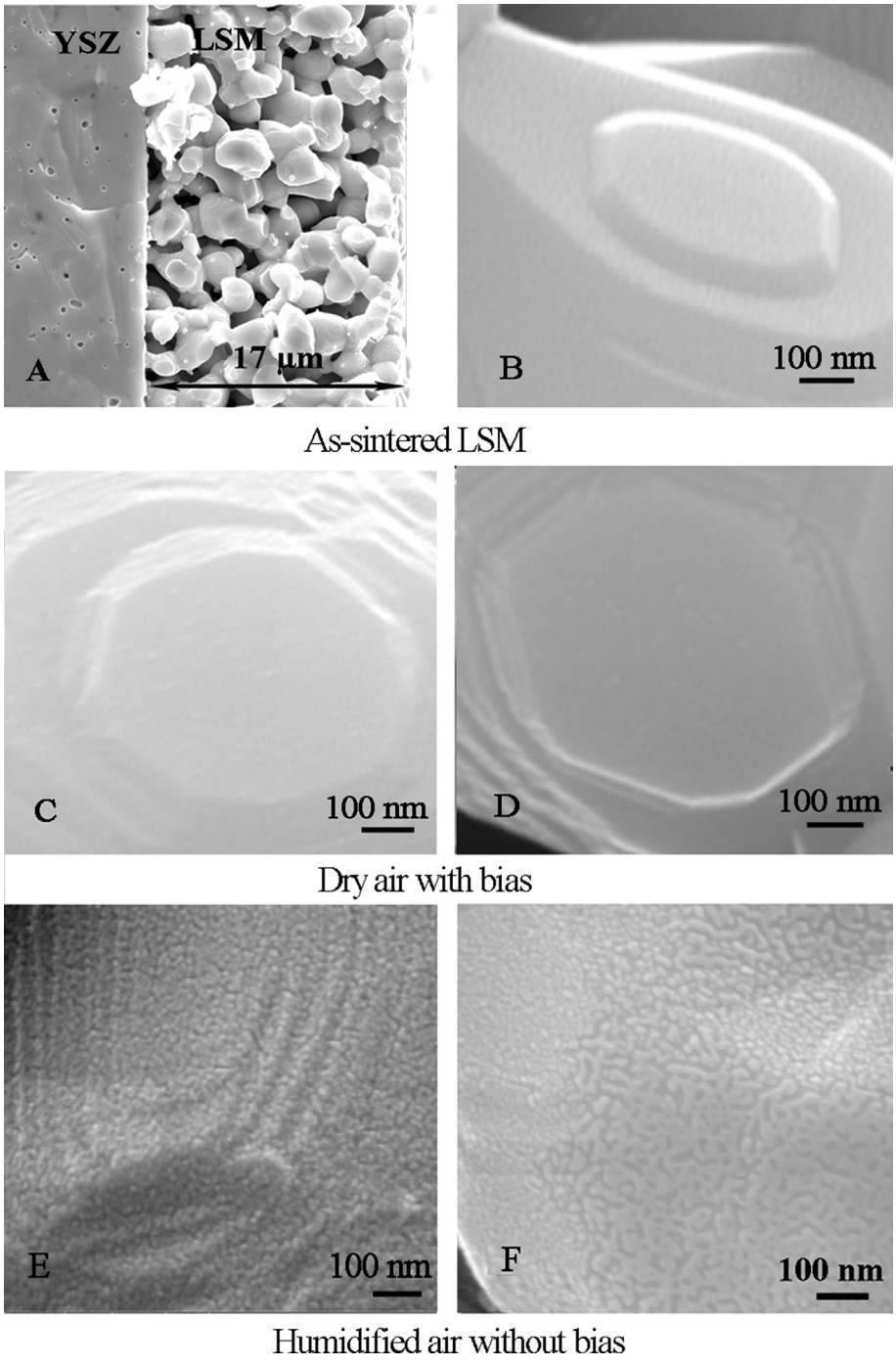

Fig. 6. SEM images of the LSM cathode surfaces tested in dry air or humidified air. A: cross section of LSM/YSZ cathode, B: sintered LSM at 1200 °C for 2 h, C, D: in dry air with a bias of 0.5 V for 100 h, at 750 °C and 850 °C, respectively. E, F: in 50% water in air with no bias for 100 h, at 750 °C and 850 °C, respectively. G, H, and I: in 3%, 10%, 50% H_2O at 850 °C with 0.5 V bias for 100 h, no additional oxygen. J: in 50% water in air at 850 °C with a bias of 0.5 V for 100 h, and the O_2 content is 21%.

$((La_{0.8}Sr_{0.2})_{0.98}MnO_{3+\delta})$ [31–33]. Since the close-packed ABO_3 perovskite structure does not accept oxygen interstitials, the oxygen excess is instead due to removal of oxygen vacancies and formation of cation vacancies (Equations (1) and (2)) [33].

$$V_o^{\bullet\bullet} + 2Mn_{Mn}^{x} + 0.5O_2 \leftrightarrow 2Mn_{Mn}^{\bullet} + O_0 \quad (1)$$

$$\text{nil} \leftrightarrow V_{La}^{'''} + V_{Mn}^{'''} + 3V_o^{\bullet\bullet} \quad (2)$$

Using Kroger–Vink notation, the combined Equations (1) and (2) can be expressed as:

$$6Mn_{Mn}^{x} + 3/2O_2 \leftrightarrow V_{La}^{'''} + V_{Mn}^{'''} + 6Mn_{Mn}^{\bullet} + 3O_0 \quad (3)$$

$Mn_{Mn}^{\bullet}$ and Mn_{Mn}^{x} represent the Mn^{4+} and Mn^{3+} ions respectively, $V_{La}^{'''}$ and $V_{Mn}^{'''}$ represent cation vacancies, and $V_o^{\bullet\bullet}$ and O_0 represent oxygen vacancies and oxygen in lattice sites, respectively. SrO and manganese oxides segregate on the LSM surface during sintering at 1200 °C [20]. During the activation process of LSM under a cathodic bias in dry air, the outermost surface SrO layer is incorporated into the LSM lattice structure with concomitant reduction of Mn ions.

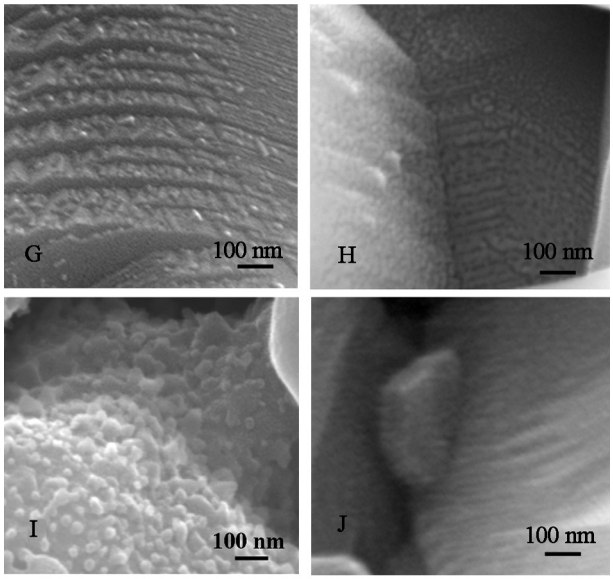

Fig. 6. (*continued*).

$$V_{La}''' + SrO + 3Mn_{Mn}^{\bullet} + e' \leftrightarrow Sr_{La}' + 0.5O_2 + 3Mn_{Mn}^{x} \quad (4)$$

Sr_{La}' represents Sr at the La sites. The equilibrium constant of this reaction assumes the form:

$$K1 = [Sr_{La}'][O_2]^{0.5}[Mn_{Mn}^{x}]^3 / \left(\left[V_{La}''' \right] [SrO] [Mn_{Mn}^{\bullet}]^3 \right)$$

Under cathodic bias, due to the existence of cation vacancies in LSM, this incorporation process is fast and leads to the initial non-ohmic resistance decrease (Fig. 3) [17,31]. It cannot be ruled out that a locally reduced LSM area becomes oxygen deficient at the LSM/YSZ interface, and oxygen incorporates into YSZ via oxygen vacancies in LSM [17,22]. Due to SrO incorporation into the LSM lattice, SrO particles were not identified on the LSM surface after testing in dry air.

The morphology of the LSM cathode surface changed significantly in humidified air. The sizes of segregated particles increased with water content, operating temperature, and bias. The segregated particles were distributed on the outer LSM cathode surface and interior surfaces. The XRD patterns show that $Sr(OH)_2$ formed on the LSM cathode. At the cell operating conditions greater than 700 °C, $Sr(OH)_2$ is not stable, and SrO will be the predominant phase (Equation (5)) [34]. The results of XPS and SEM–EDS analyses further indicate the enrichment of Sr on the LSM surface. The presence of $Sr(OH)_2$ in XRD is due to SrO reacting with H_2O when the LSM cathode was cooled down in humidified air.

$$SrO + H_2O \underset{>700\ ^\circ C}{\leftarrow} \overset{<400\ ^\circ C}{\rightarrow} Sr(OH)_2 \quad (5)$$

The effect of forming SrO on the LSM electrical performance has been demonstrated in the changes of element values in the EIS equivalent circuits. The elements of the equivalent circuits

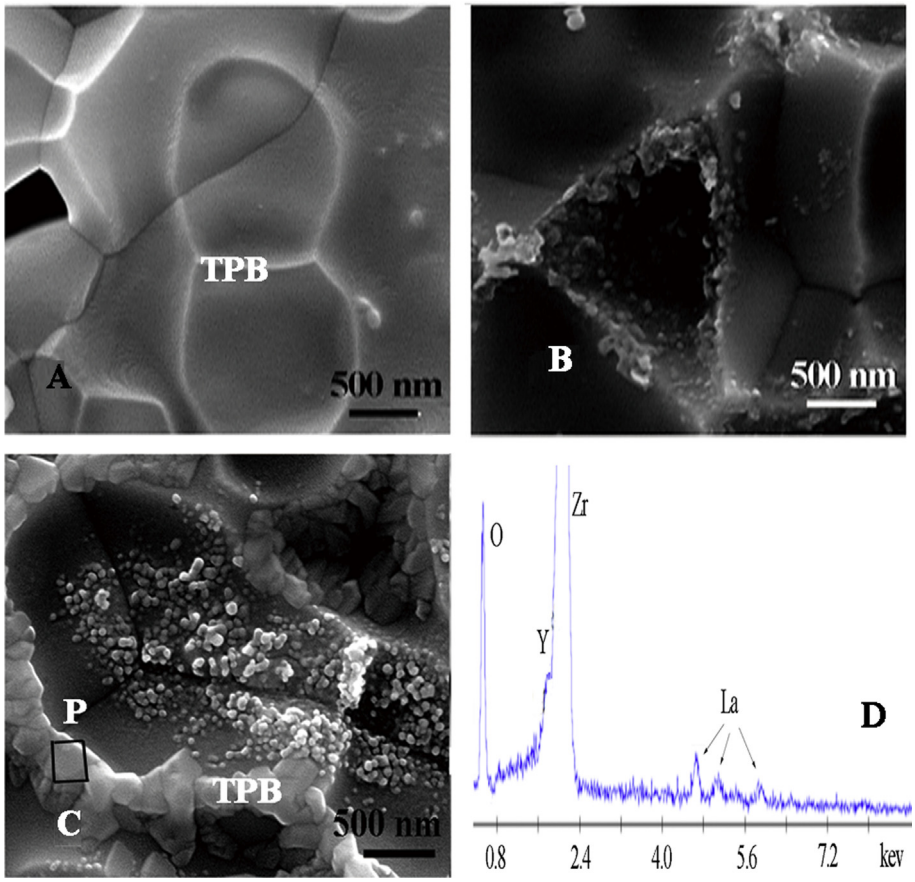

Fig. 7. SEM images and EDS spectra of the as-fabricated and post-test cathodic LSM/YSZ interfaces. A: as-fabricated. B: tested in dry air at 850 °C with a bias of 0.5 V. LSM electrode was removed by etching in 37% HCl solution for 6 h and washed with DI water, C: after testing in 50% water in air at 850 °C with a bias of 0.5 V for 100 h, D: EDS spectrum of the selected area P.

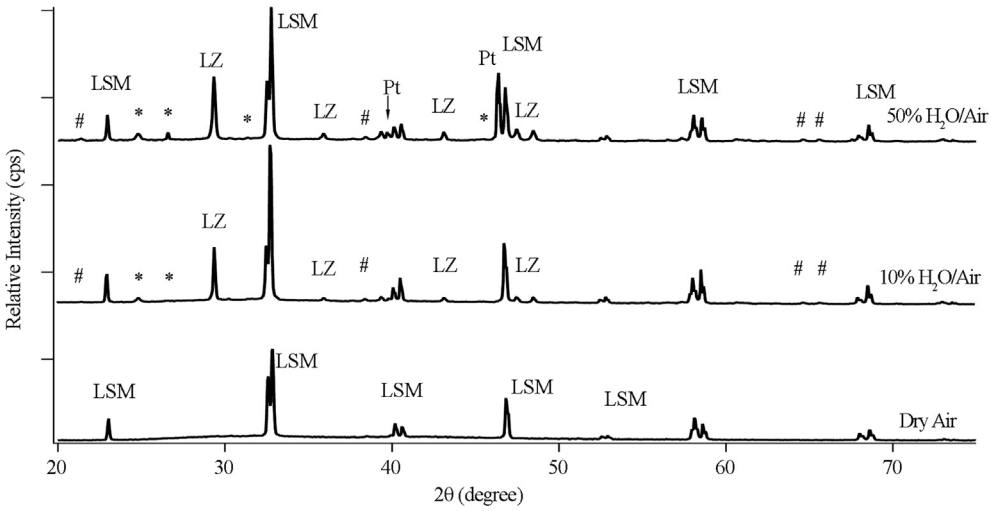

Fig. 8. XRD patterns of the post-test LSM cathode exposed in dry air, 3%, 10%, and 50% water in air for 100 h with a bias of 0.5 V. The peak assignments are LSM: $La_{0.8}Sr_{0.2}MnO_3$, LZ: $La_2Zr_2O_7$ (50–837), *: $Sr(OH)_2$(19–1276), #: Mn_2O_3 (41–1442). Pt is from platinum paste. The LSM cathode of the post-test cell in 3% H_2O/air was not detached from the YSZ electrolyte.

characterize the reactions of adsorbed species (oxygen and water) at the electrified interface [35,36]. In a 3-h test at moderate temperature (800 °C), the small increases of the *R*2 and *C*2 values (Table 1) indicate that the oxygen adsorption and oxygen ion transport are impeded by high water content, though the values of *R*3 and *R*4 are relatively stable. In a 100-h test in 50% water in air at 850 °C, the significant increase of *R*3 (Table 1) with time reflects the increase of the thickness of the surface compounds. Simultaneously, the oxygen reduction resistance *R*4 increased by about 6 times.

The mechanisms of SrO formation in humidified air are described both with and without bias. Without a bias, H_2O molecules compete with O_2 molecules to adsorb on the LSM cathode (Fig. 10A). Similar to the observations made on the nonstoichiometric compound $TiO_{2\pm x}$. Adsorbed H_2O molecules react with LSM at the surface leading to the formation of lanthanum/manganese vacancies (Fig. 10B) [37]. At high water content, the predominant defects become protons, which are compensated by lanthanum vacancies. This reaction is an endothermic reaction and is more favored at high temperature [38]. Due to increased cation vacancy formation, metal ions segregate. Segregation of Sr^{2+} proceeds first due to its large ionic radii (1.18 Å) compared to Mn^{3+} (0.72 Å) and La^{3+} (1.03 Å) [30]. Further reaction with $OH_O^{\bullet}$ leads to SrO formation at above 700 °C (Equation (6)) [34].

Table 2
XPS data of as-fabricated and post-test LSM cathodes in humidified air.

Sample	Sr/La	Sr/(Mn + La)	Binding energy (eV)		
	Molar ratio	Molar ratio	Sr 3d5/2	Mn 2p3/2	La 3d5/2
Pre-test LSM	0.23 ± 0.01	0.13 ± 0.01	132.3 ± 0.2	641.1 ± 0.5	833.9 ± 1.1
Post-test LSM[a]	0.34 ± 0.02	0.21 ± 0.01	132.8 ± 0.2	641.6 ± 0.5	834.3 ± 1.1
Post-test LSM[b]	0.58 ± 0.04	0.24 ± 0.01	132.7 ± 0.2	641.7 ± 0.5	835.1 ± 1.1
Post-test LSM[c]	1.89 ± 0.09	0.76 ± 0.04	132.8 ± 0.2	642.5 ± 0.5	835.4 ± 1.1

Other conditions are the same: 0.5 V of bias and 850 °C for 100 h.
[a] 10% H_2O.
[b] 20% H_2O.
[c] 50% H_2O.

$$H_2O + Sr'_{La} + 2O_o \rightarrow SrO + V'''_{La} + 2OH_o^{\bullet} \quad (6)$$

This SrO formation on LSM is accelerated at a relatively high temperature and high water content.

With applied cathodic bias in humidified air, the adsorbed oxygen and water molecules are postulated to undergo different but interrelated reaction pathways. The oxygen reduction pathway follows (dissociative) adsorption, surface diffusion, and charge transfer mostly at the surface of LSM [21,39]. Oxygen ions are then incorporated into the YSZ electrolyte. Simultaneously, water adsorption proceeds on the LSM surface, and adsorbed water is reduced to OH^- (Equation (7)).

$$1.5H_2O + 0.75O_2 + 3e' \rightarrow 3OH_o^{\bullet} + V'''_{La} + V'''_{Mn} \quad (7)$$

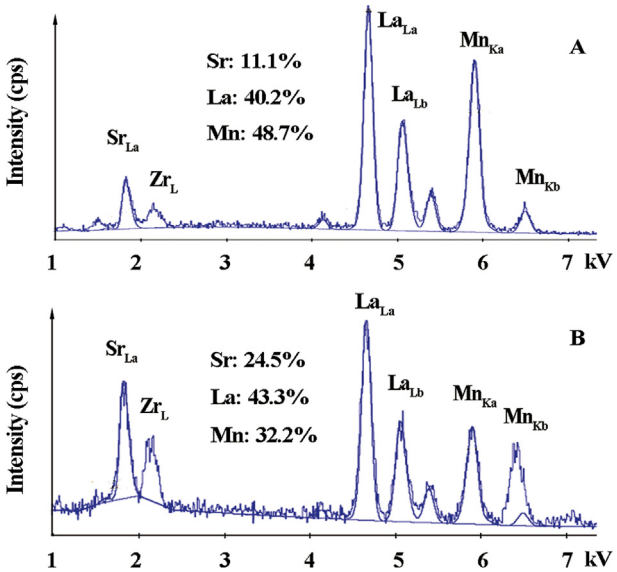

Fig. 9. SEM–EDS spectra of the as-fabricated and post-test LSM cathode surface. A: as-fabricated LSM on YSZ disc, B: post-test LSM cathode surface after testing at 850 °C in 50% H_2O in air with a bias of 0.5 V for 100 h.

Table 3
Trends of SrO formation at different operating conditions.

	Increased p_{H_2O}	Increased p_{O_2}	Increased bias	Increased temperature
Wet air	Increased	Decreased	Increased	Increased
Dry air	None	None	None	None

$OH_o^{\bullet}$ represents a proton associating with the lattice oxygen (Fig. 10B). This results in additional SrO segregation via Equation (8):

$$1.5Sr'_{La} + 3OH_o^{\bullet} + V'''_{Mn} \rightarrow 1.5SrO + 1.5H_2O + 0.5V'''_{La} \quad (8)$$

The equilibrium constant of this reaction assumes the form:

$$K2 = \left([SrO]^{1.5}[H_2O]^{1.5}\left[V'''_{La}\right]^{0.5}\right)/\left(\left[Sr'_{La}\right]^{1.5}\left[OH_o^{\bullet}\right]^{3}\left[V'''_{Mn}\right]\right)$$

Equations (7) and (8) are combined to form the following overall reaction:

$$Sr'_{La} + 0.5O_2 + 2e' \rightarrow SrO + V'''_{La} \quad (9)$$

With the water content increasing from 3% up to 50%, increasing $OH_o^{\bullet}$ (Equation (8)) leads to more SrO. Formation (Equation (8)) and removal (Equation (4)) of SrO are in competition, so the operating temperature ultimately determines whether or not the SrO particles form on LSM in humidified air. The SrO particles formed at 850 °C are much larger than those formed at 750 °C, indicating that high operating temperature favors SrO formation. Therefore, the overall effects of the reactions (7) and (8) are toward the SrO growth on the LSM cathode at 850 °C with 50% water in air. The resistances increase with time as shown in Fig. 5, indicating that the SrO growth on LSM cathode impedes the oxygen reduction.

The $R1$ at 850 °C should be smaller than that at 750 °C in the absence of compound formation at the LSM/YSZ interface. Our observations, however, show that $La_2Zr_2O_7$ and Mn_2O_3 forms more readily at 850 °C leading to an increase in the $R1$. The formation of insulating compounds increases the value of $R1$ at 850 °C as shown in Fig. 4. Formation of SrO at the LSM surface as well as the temperature affect the adsorption of water. No correlation between the $C2$ (Table 1) values and operating temperatures has been observed possibly due to the inhomogeneous distribution of SrO at the LSM surface.

As shown in Figs. 3 and 6, an increase in O_2 content shows lower increase of Rp and SrO formation indicating reduction in the cathode degradation. This is hypothesized to be due to higher p_{O_2} that results in the reduction of water adsorption with a subsequent reduction in proton production and incorporation into the LSM lattice.

The formation of $La_2Zr_2O_7$ and MnO_x is not evident in the XRD patterns of the post-tested LSM cathode in dry air (Fig. 8), in agreement with the observations of Keane et al. [40]. At higher temperature, however, it is well known that $LaMnO_3$ and ZrO_2 do not co-exist without the formation of a $La_2Zr_2O_7$ layer (Equation (10)) [41].

$$2LaMnO_3 + 2ZrO_2 \rightarrow La_2Zr_2O_7 + Mn_2O_3 \quad (10)$$

In this study, $La_2Zr_2O_7$ and Mn_2O_3 form at the LSM/YSZ interface in humidified air as reported in literature in high water content [10,42]. The SEM images (Fig. 7) and XRD patterns (Fig. 8) confirm that humidity promotes the formation of $La_2Zr_2O_7$ and Mn_2O_3. Presence of less conductive metal oxides ($La_2Zr_2O_7$ and Mn_2O_3) at the LSM/YSZ interfaces result in ohmic and non-ohmic loss, leading to degradation in the cathode electrical performance.

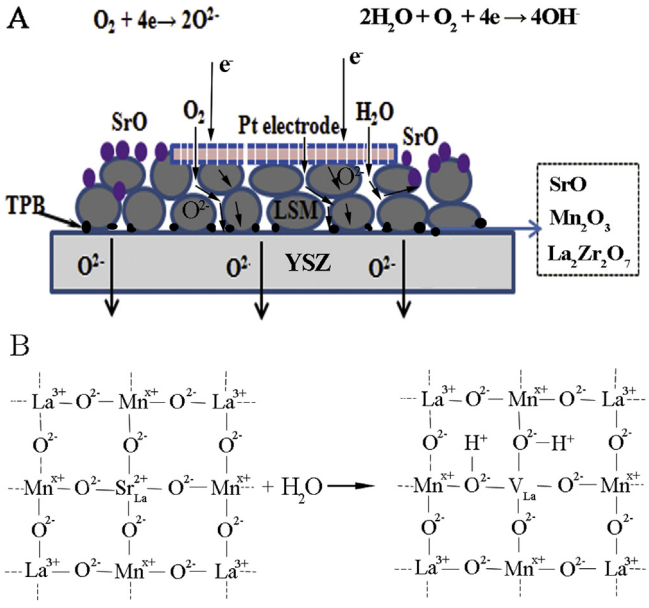

Fig. 10. Illustration of the degradation of an LSM electrode in humidified air (A) and the formation of lanthanum vacancies due to the reaction of water and LSM (B).

5. Conclusions

The morphological and structural stability of LSM cathodes has been examined under dry and humidified air (0–50%) exposure conditions using LSM/YSZ/LSM symmetric cells. Formation of SrO particles is observed at temperatures of 750–850 °C in high water content (50%) without applying a bias. Increased water content, temperature, and electric bias, or low oxygen partial pressure, lead to the formation of more SrO at the LSM surface and $La_2Zr_2O_7$ and Mn_2O_3 at the LSM/YSZ interface. EIS spectra and their equivalent circuits showed that electrical performance degradation is mainly attributed to such compound formation on LSM cathodes.

Acknowledgments

The technical work reported in this paper was performed under a research grant from the Office of Fossil Energy, US Department of Energy (DE-FE-0009682). Technical discussion with Dr. Jeff Stevenson is acknowledged. Authors sincerely thank Dr. Heng Zhang of the Institute of Materials Science, University of Connecticut for the XPS analysis. Na Li and Le Ge are acknowledged for helpful discussions and assistance with laboratory experiments.

References

[1] A. Fuerte, R.X. Valenzuela, M.J. Escudero, L. Daza, J. Power Sources 196 (2011) 4324–4331.
[2] M.D. Gross, J.M. Vohs, R.J. Gorte, J. Mater. Chem. 17 (2007) 3071–3077.
[3] P. Singh, N.Q. Minh, Int. J. Appl. Ceram. Technol. 1 (2004) 5–15.
[4] H. Yokokawa, H.Y. Tu, B. Iwanschitz, A. Mai, J. Power Sources 182 (2008) 400–412.
[5] C. Graves, S.D. Ebbesen, M. Mogensen, Solid State Ionics 192 (2011) 398–403.
[6] R.F. Tian, J. Fan, Y. Liu, C.R. Xia, J. Power Sources 185 (2008) 1247–1251.
[7] K.F. Chen, Z. Lu, X.J. Chen, N. Ai, X.Q. Huang, X.B. Du, W.H. Su, J. Power Sources 172 (2007) 742–748.
[8] J.A. Schuler, H. Yokokawa, C.F. Calderone, Q. Jeangros, Z. Wuillemin, A. Hessler-Wyser, J. Van Herle, J. Power Sources 201 (2012) 112–120.
[9] N. Sakai, K. Yamaji, T. Horita, Y.P. Xiong, H. Kishimoto, M.E. Brito, H. Yokokawa, Solid State Ionics 176 (2005) 2325–2330.
[10] J. Nielsen, A. Hagen, Y.L. Liu, Solid State Ionics 181 (2010) 517–524.
[11] E. Bucher, W. Sitte, F. Klauser, E. Bertel, Solid State Ionics 208 (2012) 45–51.
[12] A.B. Stambouli, E. Traversa, Renew. Sust. Energy Rev. 6 (2002) 433–455.

[13] L.G.J. de Haart, J. Mougin, O. Posdziech, J. Kiviaho, N.H. Menzler, Fuel Cells 9 (2009) 794–804.
[14] A. Hagen, K. Neufeld, Y.L. Liu, J. Electrochem. Soc. 157 (2010) 1343–1348.
[15] S.H. Kim, K.B. Shim, C.S. Kim, J.T. Chou, T. Oshima, Y. Shiratori, K. Ito, K. Sasaki, J. Fuel Cell Sci. Technol. 7 (2010).
[16] M. de Ridder, A.G.J. Vervoort, R.G. van Welzenis, H.H. Brongersma, Solid State Ionics 156 (2003) 255–262.
[17] W. Wang, S.P. Jiang, Solid State Ionics 177 (2006) 1361–1369.
[18] S.P. Jiang, J.G. Love, Solid State Ionics 138 (2001) 183–190.
[19] W. Lee, Z. Cai, B. Yildiz, ECS Trans. 45 (2012) 405–412.
[20] H. Jalili, J.W. Han, Y. Kuru, Z.H. Cai, B. Yildiz, J. Phys. Chem. Lett. 2 (2011) 801–807.
[21] N. Caillol, M. Pijolat, E. Siebert, Appl. Surf. Sci. 253 (2007) 4641–4648.
[22] A.K. Huber, M. Falk, M. Rohnke, B. Luerssen, M. Amati, L. Gregoratti, D. Hesse, J. Janek, J. Catal. 294 (2012) 79–88.
[23] R.R. Liu, S.H. Kim, S. Taniguchi, T. Oshima, Y. Shiratori, K. Ito, K. Sasaki, J. Power Sources 196 (2011) 7090–7096.
[24] T.L. Cable, S.W. Sofie, J. Power Sources 174 (2007) 221–227.
[25] J. Winkler, P.V. Hendriksen, N. Bonanos, M. Mogensen, J. Electrochem. Soc. 145 (1998) 1184–1192.
[26] V.F. Lvovich, Impedance Spectroscopy: Applications to Electrochemical and Dielectric Phenomena, John Wiley & Sons, 2012.
[27] D.M. Smilgies, J. Appl. Crystallogr. 42 (2009) 1030–1034.
[28] R.P. Vasquez, J. Electron Spectrosc. Relat. Phenom. 56 (1991) 217–240.
[29] B.R. Strohmeier, D.M. Hercules, J. Phys. Chem. 88 (1984) 4922.
[30] A. Stoklosa, B. Laskowska, J. Chem. Crystallogr. 38 (2008) 913–925.
[31] R.E. Cook, K.C. Goretta, J. Wolfenstine, P. Nash, J.L. Routbort, Acta Mater. 47 (1999) 2969–2980.
[32] J. Mizusaki, N. Mori, H. Takai, Y. Yonemura, H. Minamiue, H. Tagawa, M. Dokiya, H. Inaba, K. Naraya, T. Sasamoto, T. Hashimoto, Solid State Ionics 129 (2000) 163–177.
[33] J. Nowotny, M. Rekas, J. Am. Ceram. Soc. 81 (1998) 67–80.
[34] P. Patnaik, Handbook of Inorganic Chemical Compounds, first ed., McGraw-Hill Professional, 2002.
[35] X.J. Wu, H.Y. Ma, S.H. Chen, Z.Y. Xu, A.F. Sui, J. Electrochem. Soc. 146 (1999) 1847–1853.
[36] L. Bai, B.E. Conway, Electrochim. Acta 38 (1993) 1803–1815.
[37] J. Nowotny, T. Norby, T. Bakt, J. Phys. Chem. C 114 (2010) 18215–18221.
[38] H.J. Shin, J. Jung, K. Motobayashi, S. Yanagisawa, Y. Morikawa, Y. Kim, M. Kawai, Nat. Mater. 9 (2010) 442–447.
[39] J.L. Gerardo, S.H. Yang, ECS Trans. 7 (2007) 1041–1050.
[40] M. Keane, M.K. Mahapatra, A. Verma, P. Singh, Int. J. Hydrogen Energy 37 (2012) 16776–16785.
[41] N. Li, M.K. Mahapatra, P. Singh, J. Power Sources 221 (2013) 57–63.
[42] Y.L. Liu, A. Hagen, R. Barfod, M. Chen, H.J. Wang, F.W. Poulsen, P.V. Hendriksen, Solid State Ionics 180 (2009) 1298–1304.